https://dx.doi.org/10.1016/j.engstruct.2019.109604
This is the Pre-Published Version.

Experimental assessment of the flexural behaviour of concrete-filled steel tubular beams with octagonal sections

Junbo Chen, Tak-Ming Chan*

Dept. of Civil and Environmental Engineering, The Hong Kong Polytechnic University, Hung Hom, Hong Kong, China
*tak-ming.chan@polyu.edu.hk

Abstract: This paper presents an experimental investigation into concrete-filled steel tubular beams with octagonal cross-sections (OCFST) under monotonic or cyclic flexural loading. A total of eight tests, including four cyclic specimens and four monotonic counterparts, were conducted. Three concrete grades with measured compressive cylinder strength (f_c') varying from 54.5 MPa to 105.6 MPa were used to infill the OCFST specimens. The failure modes, ultimate bending moments, effective flexural stiffness, cumulative dissipated energy and deteriorations of test specimens were discussed. Test results indicate that OCFST beams exhibit a ductile plastic mode and excellent energy dissipation. Concrete grades seem to have limited influence on the ultimate strength and energy dissipation capacity. The comparison results of the ultimate bending moments and effective flexural stiffness between predictions using EN 1994-1-1 and AISC 360-16 and test results reveal their applicability to the design of OCFST beams. An energy-based hysteretic rule was adopted to assess the strength and stiffness deteriorations of the OCFST beams, and the results indicate that the predictions match well the test observations.

Keywords: Concrete-filled steel tube; Cyclic tests; Beams; Octagonal sections; Seismic effects.

1. Introduction

Concrete-filled steel tubes (CFSTs) represent an economical type of columns that have structural advantages over either conventional reinforced concrete (RC) columns or steel columns. In CFST members, the outer steel tube provides confinement to the concrete core (increasing the compressive resistance) while in turn the concrete core restrains the buckling of steel tubes (fully exerting the material strength). In addition to potential strength enhancement, the application of CFST members could also accelerate construction process by eliminating formworks. Over the past few decades, extensive experimental investigations on CFST members have been carried out to advance the knowledge of their structural behaviours under different loading conditions. Test databases have been developed by different research groups, such as Goode [1,2], Hajjar [3] and Liew et al. [4]. The results indicate that CFST members have favourable load-bearing capacity and excellent ductility and lead to the development of design provisions in design codes such as AISC 360-16 [5] and EN 1994-1-1 [6]. Moreover, cyclic test results of CFST members indicate that CFST members have relatively larger energy dissipation capacity and comparatively lower strength and stiffness deteriorations under cyclic loading compared with RC and steel tubular counterparts.

The most important advantage that CFST members have over conventional RC members is the confinement to the concrete core by the steel tubes. Distinct behaviours in respect to the confinement effect have been found with different cross-sectional shapes. To date, majority of the research carried out regarding CFST members has focussed on square, rectangular and circular sections, which are the generally used cross-sectional shapes in construction industry. An extensive test database consisting 3103 tests was newly compiled by Thai et al. [7]. This database contains rectangular and circular CFST columns under axial compression and combined axial force and bending moment. The test results were compared with the predictions obtained from different codes of practice to evaluate the applicability to extend current design rules to the design of high strength materials. Regarding the flexural behaviour of CFST beams, comprehensive analyses have been conducted and the plastic stress distribution method was found viable to design CFTS beams [8-12]. Xiong et al. [12] reviewed existing CFST beam tests and developed a test database containing 16 circular CFST beams and 54 square/rectangular

© 2019. This manuscript version is made available under the CC-BY-NC-ND 4.0 license http://creativecommons.org/licenses/by-nc-nd/4.0/

CFST beams. Subsequently, eight specimens made up from high strength materials (steel yield strength up to 779 MPa and concrete cylinder strength up to 183 MPa) were tested to assess the current design codes.

CFST members with elliptical or polygonal section columns are sometimes used as well due mainly to the aesthetic or functional considerations [13], and also have attracted the interests of researchers. A number of research investigations focusing on the elliptical CFST members have been conducted, including cross-section stub columns behaviour [14-15] and member beam-columns behaviour [16-17]. Steel tubes with polygonal cross-sections in particular have been commonly used in telecommunication structures [18]. The applications of polygonal cross-sections, such as hexagonal and octagonal cross-sections, in composite structures have also attracted the attention of researchers. Extensive literature reviews on the octagonal CFST stub column tests are presented by Chen et al. [19], Zhu and Chan [21]. However, most of the existing literature for octagonal CFSTs have focussed on stub columns. Research on the structural behaviour of octagonal CFST members under flexural loading is extremely scarce. To promote the application of polygonal steel tubes in CFST structures, it is of great interest to advance the knowledge of the flexural behaviour of octagonal CFST members.

The primary focus of this paper, following the research [19-21], is to experimentally investigate the flexural behaviour of CFST beams with octagonal cross-sections under monotonic or cyclic flexural loading. A total of eight octagonal beams, including six CFST beams infilled with three different concrete grades (with concrete cylinder strength varying from 54.5 MPa to 105.6 MPa) and two hollow section counterparts, were tested under either monotonic or cyclic loading. The experimental results with regard to the failure modes, ultimate bending strengths, effective flexural stiffness, cumulative dissipated energy and deteriorations are discussed.

2. Experimental programme

2.1 General

To evaluate the flexural behaviour of octagonal CFST beams under either monotonic or cyclic loading, six OCFST beams infilled with three different concrete grades as well as two hollow section counterparts were tested, four of which were tested under monotonic loading, while the other four were under cyclic loading. The target compressive cylinder strengths of the three different concrete grades were 30 MPa (C30), 60 MPa (C60), and 90 MPa (C90), with measured compressive cylinder strengths at test day of 54.5 MPa, 78.5 MPa, and 105.6 MPa respectively. Using different concrete grades also achieved different values of the steel contribution ratio (δ) specified in EN 1994-1-1 and defined according to Eq. (1), where A_s and A_c are cross-sectional areas of the steel tube and the concrete core, respectively, f_y and f_c' are the yield strength of the steel tube and the concrete compressive cylinder strength, respectively.

$$\delta = \frac{A_s f_y}{A_s f_y + A_c f_c'} \tag{1}$$

The octagonal steel tubes were manufactured from steel plates with a nominal thickness of 4 mm and with a nominal yield strength of 355 MPa by a local fabricator. The fabrication route involves a combination of press-braking and welding as shown in Fig. 1 (same approach as in [19]). All beam specimens were designed having the same dimensions with the nominal diameter of the circumcircle (D) of 150 mm and the overall width (h) of 140 mm respectively. The actual dimensions of the cross-section of each specimen were precisely measured and the average values of the measured diameter of the circumcircle (D), overall width (h), width of flat side (B), width of flat side excluding corner portions (b) and thickness (t), as well as the detailed information of the test specimens including material parameters are summarised in Table 1.

The hollow section specimens were labelled as HM or HC, where the first letter "H" stands for hollow section and the second letter "M" or "C" stands for either monotonic or cyclic flexural loading. In the designation of OCFST specimens, the first letter "C" is for concrete-filled section, followed by two digital numbers standing for the concrete grade in terms of concrete cylinder strength, and the fourth letter refers to the type of flexural loading, where M" or "C" stands for either monotonic or cyclic flexural loading, respectively.

Regarding the cross-section slenderness of octagonal sections, no design rule is specified in the American codes for static design: AISC 360-16 [5] and for seismic design: AISC 341-16 [22], nor in the corresponding European codes for static design: EN 1994-1-1 [6], and for seismic design: EN 1998-1 [23]. In this paper, the slenderness limit for plate buckling in octagonal cross-section proposed by Zhu et al. [24] ($b/t \le 29.8\sqrt{235/f_y}$) was used to assess the classification of the octagonal section in this test programme. The results indicate that the octagonal sections could be classified as Class 1-3 when the measured yield strength together with the measured *b* and *t* values (Table 1) were considered.

2.2 Material tests

Three tensile coupons were extracted from the flat portions in the longitudinal direction of an octagonal steel tube. These coupons were tested in accordance with EN ISO 6892-1[25] in an in-house Instron 8803 Fatigue Testing System with a capacity of 500 kN. The basic material properties, namely elastic modulus (E_s), yield strength (f_y), ultimate tensile strength (f_u), the yield strain (ε_y), the strain when strain hardening initiates (ε_{st}), the strain corresponding to the ultimate tensile strength (ε_u) and the elongation at fracture based on the original gauge length (ε_f), obtained from coupon tests are listed in Table 2. Full stress-strain curves up to fracture of the three tensile coupon tests are presented in Fig. 2.

Commercial concrete produced by a local concrete producer was used and the concrete mix proportions of the used three concrete grades, based on saturated surface dry (SSD) condition, are listed in Table 3. Three standard concrete cylinders with a diameter of 150 mm and a height of 300mm were prepared during the concrete infilling of specimens for each concrete grade. The cylinders were tightly wrapped with cling film and sealed with tape to keep the moisture content and to simulate the curing conditions of the concrete that were infilled in the tubes. These cylinders were stored at normal daily temperatures besides the specimens to ensure the cylinders experienced the similar conditions as the specimens experienced. The cylinders were tested at the test day to obtain the exact concrete strengths at the test day. Four strain gauges with a gauge length of 90 mm were attached to the surface of the standard cylinders at 90-degree to each other to obtain the stress-strain curves and the elastic modulus of concrete. The concrete cylinders were tested under displacement-control at a rate of 0.2 mm/min and the testing procedure complied with EN 12390-3 [26]. The concrete compression test results, i.e. the compressive cylinder strengths (f_c') and the elastic modulus (E_c), are summarised in Table 1.

2.3 Test setup, instrumentation and loading protocol

The specimens were tested in a reaction frame at the structural laboratory of The Hong Kong Polytechnic University. Schematic and experimental views of the test setup are presented in Fig. 3. A roller-roller boundary condition at both ends of the beams was achieved, with an effective testing length, L_f, of 962 mm (see Fig. 3(a)). The monotonic or cyclic lateral load was applied to the specimen at mid-span using a servo-controlled hydraulic actuator with a maximum stroke of 300 mm and capacities of 300 kN in compression and 150 kN in tension. The monotonic or cyclic lateral load was applied using displacement control, while the cyclic loading stage was performed by controlling the lateral displacement at mid-span of the specimen.

Referring to Fig. 3(a), five linear variable displacement transducers (LVDTs) were installed to measure the corresponding displacements. LVDT 1 controlled the drift value of the tests, LVDTs 2-3 were placed to measure

the lateral displacements at specific locations, and LVDTs 4-5 measured the displacements of the end supports to confirm there was no uplift during the loading cycles. In total, eight strain gauges were mounted to the specimens. Four of the strain gauges (SG1 to SG4) were placed at the positions 20 mm and 170 mm away from the section just behind the vertical stiffeners, while the other four (SG5 to SG8) were mounted at the symmetric positions about the hydraulic actuator on the other side as shown in Fig. 3(a).

The SAC loading protocol [27], as shown in Fig. 4, was adopted to apply the lateral cyclic loads. Six cycles were applied for drift ratios at 0.375%, 0.50% and 0.75%, four cycles at 1%, two cycles at 1.5% and 2%, and two cycles for the remaining drift ratio levels with an increment of 1% until the failure of the specimen. The drift ratio is defined as the ratio of lateral displacement divided by the effective length (L_f = 962 mm).

3. Experimental results and discussion

3.1 Failure modes

Generally, significant outward local buckling developed at the mid-span of the beams, which was located just behind the vertical stiffeners for all specimens under monotonic or cyclic loading, as shown in Figs. 5 and 6. For the specimens under monotonic loading, it was observed that the outward bulge only formed on the compression side of the cross-section. The outward local buckling phenomenon of hollow section specimen was more obvious than that of the OCFST specimens as shown in Fig. 5, indicating that the infilled concrete could delay the occurrence of the local buckling of steel tube. For the specimens under cyclic loading, it was observed that the outward bulge was firstly initiated on the compression side after the extreme longitudinal compression strain of the steel tube exceeded the yield strain (ε_y). Subsequently, the bulge formed on the opposite side of the steel tube when the lateral load was reversed. The outward local buckling phenomenon became more obvious with the increase of the lateral displacement. The bulge then grew as a complete ring, similar to the elephant foot buckling, as depicted in Fig. 6. The specimens under cyclic loading failed by fracture of the steel tube after significant outward local buckling, which may be due to the relatively large drift ratios (more than 8%) at the end of the test for these specimens. Cracking of the steel tube initiated when the drift ratio reached around 6% and propagated with the increase of the drift until fracture.

3.2 Global lateral behaviour

The measured lateral load (P) *vs* lateral drift (Δ) curves were used to examine the global lateral behaviour of the OCFST beam specimens as plotted in Fig. 7 for monotonic tests and Fig. 8 for cyclic tests. It was found that the specimens infilled with concrete developed a stable lateral load (P) *vs* lateral drift (Δ) behaviour as the lateral load increased gradually for the full plastic deformation as shown in Fig. 7, while the hollow section counterpart exhibited strength degradation at higher drift levels. The effect of concrete infilling on the improvement of the lateral load is significant compared to the hollow section counterpart with improvements of 25.2%, 25.4% and 31.6% for concrete cylinder strengths varying from 54.5 MPa to 105.6 MPa respectively (corresponding to 30 mm drift). However, the influence of the grades of infilled concrete is limited as only a 5.1% improvement on lateral load (corresponding to 30 mm drift) was achieved when increasing the concrete strength from 54.5 MPa to 105.6 MPa, further indicating that within the scope of this study the influence of the steel contribution ratio by changing concrete cylinder strength is rather limited.

It can be seen from Fig. 8 that the hollow section specimen exhibited a plump hysteretic curve, however, the specimens infilled with concrete developed hysteretic curves with slight pinching effect. The occurrence of pinching is largely due to the opening of the cracks on the tension side and the closing of the cracks on compression side after the propagation of the vertical cracks in concrete core. The strength of all the cyclic

specimens deteriorated at higher drift levels during the cyclic loading due to the cumulative local buckling phenomenon and material damages.

3.3 Strain analysis

Figs. 9-10 present the lateral load versus strain curves of typical specimens, namely HC (hollow section) and C90C (infilled with C90 concrete). The yield strain (ε_y) of the steel obtained from the tensile coupon tests is also highlighted in these figures (please refer to Fig. 3(a) for the numbering system of the strain gauges). It can be observed that the lateral load and strain relations show a linear range in the initial loading stage. After yielding of the steel, strains measured by SG1 and SG2 (see Figs. 9(a-b) and 10(a-b)) increased dramatically and residual strains could be observed upon unloading, indicating that local buckling initiated and developed significantly. It is noted that the strains measured by SG1 and SG2 increased much faster than the strains measured by SG3 and SG4 (see Figs. 9(c-d) and 10(c-d)) after the steel yielded. Focusing on the strains measured by SG3 and SG4, it is clear that the strains just reached and moderately exceeded the yield strain, indicating that the plastic hinge length exceeded 170 mm (around 1.1h).

3.4 Local behaviour

3.4.1 Experimental observations

The local behaviour of the plastic hinge region of the OCFST specimens was examined on the basis of the moment (M) at mid-span of the beam *vs* the drift ratio (θ) curves, which were plotted in Fig. 11 for monotonic tests and Fig. 12 for cyclic tests. The drift ratio (θ) is defined as the ratio of lateral drift at mid-span over the effective length (L_f). The moment at mid-span was calculated as the moment induced by the lateral load, as expressed by Eq. (2), where P is the recorded lateral load.

$$M = \frac{1}{2} P \cdot L_f \tag{2}$$

As depicted in Fig. 11, the moments of OCFST beam specimens increase gradually with the increase of drift ratio up to a relatively large drift ratio around 0.1. In this case, it is difficult to determine the representative ultimate bending capacity. Majority of researchers simply reported the maximum loads obtained at a very large deformation, most likely at the end of test. From a practical design's point of view, reporting the loads occurred at very large deformation is not safe, in particular when the loads are used to derive or validate design equations, because such a large strain could not be reached in real structures. Therefore, Han [8] suggested the bending capacity should be determined when the strain of extreme fibre on tension side reaches 0.01 to avoid excessive deformation. In this study, to address this issue, resistances when the strain of extreme tension fibre reached 0.01 ($M_{1\%}$), corresponding to 0.02 drift ratio ($M_{2\%}$) and 0.04 drift ratio ($M_{4\%}$), as well as the maximum values (M_{Max}) were reported, as summarised in Table 4.

All cyclic specimens exhibited plump hysteretic curves as shown in Fig. 12. Slight pinching was observed for the specimens infilled with concrete. The maximum moments (M_{ue}) of all the cyclic specimens obtained from the test results, which were taken as the average values of the maximum moments in the push and pull directions, are listed in Table 5. It can be concluded that, with the infill of concrete, the improvement in the bending moments over the hollow specimen is significant, 18.8%, 20.1%, and 21.1% when the infilled concrete strength varied from 54.5 MPa to 105.6 MPa. Comparing the specimens infilled with different concrete grades, the results indicate that the increase of the ultimate bending moment due to the increase of concrete strength is limited in comparison to the increase in the axial compression capacity. For instance, when the concrete cylinder strength changes from 54.5 MPa to 105.6 MPa, the increase in the ultimate bending moment (M_{ue}) is only around 2%

(please refer to Table 5). Due to the brittle nature of concrete, concrete in tension region has limited contribution to the moment resistance. If the tensile strength of concrete is neglected, the neutral axis can be easily located by solving the equilibrium equation. When the concrete changes from normal strength concrete to high strength concrete, due to the increase in the compressive strength, the neutral axis of the composite section is expected to move upwards, which in turn reduces the area of concrete in compression region. As a result, limited improvement in the moment resistance is observed.

3.4.2 Cross-sectional resistance

As specified by EN 1994-1-1 [6], the bending moment capacity can be calculated using the plastic stress distribution method, as shown in Fig. 13, assuming that the steel reaches its yield strength in both compression and tension and the concrete in compression reaches a stress of βf_{cd}, where f_{cd} is the design concrete strength taken as f_c'/γ_c and γ_c is the partial factor for concrete, and β is a shape factor for the concrete stress block. Generally, the shape factor is taken as 0.85 for reinforced concrete and composite members. However, according to the European code, for CFST members, this factor can be taken as unity. AISC 360-16 [5] adopts different stress or strain distribution methods for the evaluation of the cross-section resistance for different cross-section classes, namely plastic stress distribution method for compact sections and strain compatibility method/elastic stress distribution method or effective stress-strain method for noncompact or slender sections. Based on the assessment of the cross-section class of octagonal section that the octagonal section is classified as Class 1-3 (stocky) as discussed in Section 2.1, the plastic stress distribution method was therefore adopted as well to evaluate the bending capacity of the OCFST beams in this paper. AISC 360-16 applies different values of the shape factor for circular and square/rectangular CFST beam-columns, i.e. 0.95 for circular sections and 0.85 for square/rectangular sections. As the American code does not prescribe any value for octagonal sections, in this paper, a shape factor of 0.95 was assumed to evaluate the bending capacity according to AISC 360-16.

The ultimate bending moments of the OCFST beams obtained from the tests were compared with those predictions from EN 1994-1-1 and AISC 360-16 to examine the applicability of the two codes in predicting the flexural strength of OCFST beams. It should be stated that high strength concrete is not covered in EN 1994-1-1 ($f_c' < 50$ MPa) and AISC 360-16 ($f_c' < 69$ MPa). However, in this study, the equations specified in these codes were still used to examine their applicability for high strength concrete. Furthermore, to allow for a direct comparison, all partial safety factors were set to unity. Therefore, measured f_c' was used instead of f_{cd} while evaluating the bending moment capacity.

The comparison results of the monotonic tests are listed in Table 4, indicating that the reported bending moments, $M_{1\%}$ and $M_{2\%}$, are very close to the predictions using EN 1994-1-1 ($M_{pl,Rd}$) and AISC 360-16 (M_{AISC}) with the mean values varying from 0.989 to 1.019, which means the bending moments obtained when the strain of extreme tension fibre reached 0.01 ($M_{1\%}$) and corresponding to 0.02 drift ratio ($M_{2\%}$) are comparable with the predictions using the plastic stress distribution method. If the reported maximum bending moments were considered, code predictions were found to predict the capacities on the conservative side with an overall mean value of $M_{max}/M_{pl,Rd}$ equal to 1.175 with the corresponding COV of 0.068, where M_{max} is the reported maximum ultimate moments obtained from test results and $M_{pl,Rd}$ is the ultimate moments predicted using EN 1994-1-1. The shape factor (β) used in AISC 360-16 was 0.95, relatively smaller than unity used in EN 1994-1-1, the comparison result is therefore slightly conservative with an overall mean value of M_{max}/M_{AISC} equal to 1.185 with the corresponding COV of 0.072. The comparison results of the cyclic tests are summarised in Table 5. Results indicate that bending moments obtained when the strain of extreme tension fibre reached 0.01 ($M_{1\%}$) are comparable with EN 1994-1-1 and AISC 360-16 predictions with the mean values of 1.004 and 1.014, whilst the maximum bending moments were found to be 12.3% and 13.1% higher than EN 1994-1-1 and AISC 360-16 predictions respectively. To conclude, the bending moments corresponding to 1% extreme tensile strain $M_{1\%}$ could be used to represent the bending capacity of the OCFST beams. The applicability of EN 1994-1-1 and

AISC 360-16 to the design of OCFST beams seems to be valid and the predictions are close to the flexural resistance.

3.5 Hysteretic performance

3.5.1 Effective flexural stiffness

The flexural stiffness of the OCFST beams was evaluated by inspecting the effective cross-section flexural stiffness (K_{ie}), which is defined as the secant stiffness corresponding to the moment of $0.2M_{ue}$ for specimens under cyclic loading [28] and $0.2M_{pl,Rd}$ for specimens under monotonic loading. The effective cross-section flexural stiffness can be calculated by Eq. (3).

$$K_{ie} = \frac{0.2M_{ue} \text{ or } 0.2M_{pl,Rd}}{\phi} = \frac{0.2M_{ue} \text{ or } 0.2M_{pl,Rd}}{(\varepsilon_t - \varepsilon_c)/h} \tag{3}$$

where ϕ is the curvature corresponding to $0.2M_{ue}$ or $0.2M_{pl,Rd}$, ε_t and ε_c are the measured strains of the extreme fibres on tension and compression sides, and h is the overall width of the octagonal section. The calculation results of K_{ie} of all the specimens are listed in Table 6.

The theoretical effective flexural stiffness (K_{ic}) of a composite section can be computed according to Eq. (4), where E and E_c are elastic moduli of the steel and concrete respectively, I_s and I_c are moment of inertia of the steel tube and concrete core, respectively, α is a correction factor to reduce the gross stiffness of the concrete taking account of the cracks in the concrete [29].The factor α takes different forms in different codes of practice, e.g. a constant of 0.6 in EN 1994-1-1 and a non-constant (see Eq. (5)) in AISC 360-16, where A_s and A_g are areas of steel tube and composite section.

$$K_i = EI_s + \alpha E_c I_c \tag{4}$$

$$\alpha = 0.45 + 3A_s/A_g \le 0.9 \tag{5}$$

The effective flexural stiffness (K_i) of the OCFST beams obtained from the test results were compared with those predicted from EN 1994-1-1 and AISC 360-16 to examine their applicability in predicting the flexural stiffness of OCFST beams. The comparisons of the effective flexural stiffness are summarised in Table 6, where K_{ie} is the flexural stiffness obtained from the test results and K_{ic} is the effective flexural stiffness predicted based on design codes. The results show that EN 1994-1-1 slightly underestimates the effective flexural stiffness by around 6% with a mean value of K_{ie}/K_{ic} equal to 1.064 with the corresponding COV of 0.033, and AISC 360-16 predicted the effective flexural stiffness well with a mean value of K_{ie}/K_{ic} equal to 1.017 with the corresponding COV of 0.052, respectively.

3.5.2 Energy dissipation

The cumulative hysteresis dissipated energy (E_h) is defined as the energy that the OCFST beams dissipate during the cyclic loops and can be evaluated according to Eq. (6),

$$E_h = \sum_{i=1}^{n} (E_i^t + E_i^c) \tag{6}$$

where i is the number of cycles, n is the total number of cycles, and E_i^t and E_i^c are the energies dissipated in the ith half cycle in tension and the ith half cycle in compression, respectively.

The cumulative dissipated energy up to the termination of the test (E_h) was evaluated based on the local hysteretic behaviour (moment *vs* drift ratio curves as illustrated in Fig. 12). The cumulative dissipated energy of all the cyclic specimens is summarised in Table 6. The dissipated energies of OCFST beam specimens increased by 48.4%, 49.6%, and 51.1% respectively for different concrete grades compared to hollow specimen counterpart. However, it was found that the strength of concrete and the steel contribution ratio appear to have negligible influence on the cumulative energy dissipation.

3.5.3 Deteriorations of strength and stiffness

The strength and stiffness deteriorations of structural members during seismic excitations are a critical topic in the earthquake engineering. However, the deteriorations of CFST members have been rarely discussed in the literature. To evaluate the seismic demand of CFST members in composite structures, it is of significant importance to address this issue, as shown in Fig. 14, which depicts a comparison of the monotonic and cyclic responses of 'identical' OCFST beams in this paper. The monotonic test result exhibits a stable moment-drift ratio response and no strength deterioration is observed, whilst the cyclic hysteretic behaviour indicates that (1) strength and (2) stiffness deteriorate with the increase in the number and amplitude of cycles. The strength deterioration β_1 and stiffness deterioration β_2 [30] observed in the test, can be determined by Eqs. (7) and (8), as presented in Fig. 15.

$$\beta_1 = 1 - \frac{M_{\mathrm{i,c}}}{M_{\mathrm{i,m}}} \tag{7}$$

$$\beta_2 = 1 - \frac{K_{\mathrm{i,c}}}{K_{\mathrm{ie}}} \tag{8}$$

where $M_{\mathrm{i,c}}$ and $M_{\mathrm{i,m}}$ are the moments recorded from cyclic test in *i*th cyclic and corresponding moment in the monotonic test (on the basis of same drift ratio), $K_{\mathrm{i,c}}$ is the unloading or reloading stiffness in *i*th cyclic, K_{ie} is the flexural stiffness discussed in section 3.4.1. The strength and stiffness deteriorations of each cyclic test were therefore calculated and plotted against the normalised cumulative dissipated energy, as shown in Fig. 16. The normalised cumulative dissipated energy is the ratio of the cumulative dissipated energy over E_{pl}, as expressed in Eqs. (9) and (10),

$$\eta = \left(\sum_{j=1}^{i} E_{\mathrm{j}} \right) / E_{\mathrm{pl}} \tag{9}$$

$$E_{\mathrm{pl}} = \frac{1}{2} \cdot M_{\mathrm{pl}} \cdot \theta_{\mathrm{p}} = \frac{1}{2} \cdot M_{\mathrm{pl,Rd}} \cdot \frac{M_{\mathrm{pl,Rd}}}{K_{\mathrm{ie}}} \tag{10}$$

where η is the normalised cumulative dissipated energy, $\sum_{j=1}^{i} E_{\mathrm{j}}$ is the cumulative energy dissipated in past *i* excursions, E_{pl} is the energy dissipated when the critical section of a member reaches its full plastic moment M_{pl} is the full plastic moment of the member taken as $M_{\mathrm{pl,Rd}}$ in this paper, and θ_{p} is the drift ratio corresponding to M_{pl} taken as $M_{\mathrm{pl,Rd}} / K_{\mathrm{ie}}$, respectively, as shown Fig. 17.

It is evident from Fig. 16 that both the strength and stiffness deteriorations of the hollow specimen increase dramatically after the local buckling of the steel tube occurs and with the concrete infilled, the deteriorations are delayed due to the fact that the concrete core could delay or even eliminate the local buckling of the steel tube, hence providing better ductility and energy dissipation capacity. Moreover, due to the brittle nature of the high strength concrete, it seems the specimen infilled with higher strength concrete exhibits larger deteriorations.

Rahnama and Krawinkler [30] proposed a hysteretic rule to evaluate the rates of deteriorations on a basis of the hysteretic energy dissipated during cyclic loops. The concept of reference hysteretic energy dissipation capacity E_t was adopted in the rule. The reference hysteretic energy dissipation capacity E_t depends on the strength and rotation capacity of the member, assuming that it is an inherent property of a member independent of the loading history imposed to the members and can be expressed as a multiple of $M_y \cdot \theta_y$, i.e.:

$$E_t = \lambda \cdot M_y \cdot \theta_y \tag{11}$$

where λ is the coefficient of reference hysteretic energy dissipation capacity and is an inherent property of a member, M_y is the elastic yield moment, and θ_y is the rotation corresponding to M_y. The energy-based parameter to evaluate the deterioration is given by Eq. (12).

$$\beta = \left(\frac{E_i}{E_t - \sum_{j=1}^{i-1} E_j} \right)^c \tag{12}$$

where E_i is the hysteretic energy dissipated in the ith excursion, $\sum_{j=1}^{i-1} E_j$ is the cumulative energy dissipated in the past i-1 excursions, E_t is the reference energy dissipation capacity from Eq. (11), and c is an empirical parameter controlling the rate of deterioration. A reasonable range for parameter c is between 1.0 and 2.0, as suggested for damage modelling of steel structural members in [30]. This deterioration rule was successfully incorporated into a hysteretic model that could account for deterioration modelling of steel members by Ibarra et al. [31] and the hysteretic model for steel members was further improved by Lignos and Krawinkler [32].

The deterioration rule proposed by Rahnama and Krawinkler [30] was adopted in this paper with some modifications being made to assess the deteriorations of strength and stiffness in concrete-filled steel tubular (CFST) members. The reference hysteretic energy dissipation capacity E_t in Eq. (11) was modified for CFST members as expressed by Eq. (13).

$$E_t = \lambda \cdot M_{pl,Rd} \cdot \theta_p \tag{13}$$

where $M_{pl,Rd}$ is the plastic resistance moment of the CFST section, θ_p is the drift ratio corresponding to $M_{pl,Rd}$ taken as $M_{pl,Rd} / K_{ie}$.

Ibarra et al. [31] and Lignos and Krawinkler [32] adopted a trial-and-error process to calibrate the parameters incorporated in the hysteretic model, such as λ and c, until a satisfactory match between the test result and model prediction was achieved. Same calibration approach was utilised in this paper to calibrate the values of parameters λ and c as shown in Figs. 18 and 19. It was found that the strength and stiffness deteriorations observed in the tests could be predicted with an acceptable accuracy if the parameters λ and c are well calibrated as shown in Figs. 18 and 19.

4. Conclusion

An experimental investigation on eight CFST beams with octagonal sections (OCFST) under either monotonic or cyclic lateral load was presented in this paper. Three concrete grades with compressive cylinder strengths varying from 54.5 MPa to 105.6 MPa were used to infill the octagonal steel tubes. Based on the experimental and analytical results, it could be concluded that octagonal beams exhibit excellent ductility and energy

dissipation behaviour. A slight pinching effect was observed from the hysteretic curves of the concrete-filled specimens compared to the hollow section counterpart. With concrete infilled, the ductility and energy dissipation capacity of an octagonal beam increase. However, increasing the concrete strength has negligible effects on the ultimate bending moment and energy dissipation capacities. Within the scope of the test results presented in this study, the current design rules prescribed in EN 1994-1-1 and AISC 360-16 is applicable to the design of OCFST beams with slight underestimations of the capacity. EN 1994-1-1 and AISC 360-16 predict the effective flexural stiffness of OCFST beams quite well with an overall mean value of 1.064 and 1.017. It was also found that the strength and stiffness deteriorations of the OCFST beams could be predicted with an acceptable accuracy using the hysteretic rule proposed by Rahnama and Krawinkler [30], which provides a feasible way to quantify the deteriorations in the seismic excitation.

Acknowledgement

The authors are grateful for the support from the Chinese National Engineering Research Centre for Steel Construction (Hong Kong Branch) at The Hong Kong Polytechnic University. The authors would also like to thank the technical staff – Mr. Y.H. Yiu and Mr. M.C. Ng of the Structural Engineering Research Laboratory at The Hong Kong Polytechnic University for their assistance on the experimental works.

References

[1] Goode CD. Composite Columns - 1819 Tests on Concrete-Filled Steel Tube Columns Compared with Eurocode 4. I Struct Eng. 2008, 86: 33–38.
[2] Goode CD. Composite Column tests – Database and Comparison with Eurocode 4. I Struct Eng. 2008, 86: 33–38. In 12th International Conference on Advances in Steel-Concrete Composite Structures (ASCCS 2018), València, Spain, June 27-29, 2018; 763-767.
[3] Hajjar JF, Gourley BC, Tort C, Denavit MD, Schiller PH. Steel-Concrete Composite Structural Systems, Northeastern University, 2013.
[4] Liew JYR, Xiong M, Xiong D. Design of concrete filled tubular beam-columns with high strength steel and concrete. Struct, 2016; 8:213–226.
[5] ANSI/AISC 360-16. Specification for structural steel buildings. Chicago: American Institute of Steel Construction (AISC); 2016.
[6] EN 1994-1-1. Design of composite steel and concrete structures. Part 1–1: general rules and rules for buildings. European Standard, CEN; 2004.
[7] Thai S, Thai HT, Uy B, Ngo T. Concrete-filled steel tubular columns: Test database, design and calibration. J Construct Steel Res. 2019; 157: 161-181.
[8] Han LH. Flexural behaviour of concrete-filled steel tubes. J Construct Steel Res 2004; 60(2): 313-337.
[9] Probst AD, Kang HK T, Ramseyer C, Kim U. Composite flexural behavior of full-scale concrete-filled tubes without axial loads. J Struct Eng 2010; 136(11): 1401-1412.
[10] Prion HG, Boehme J. Beam-column behaviour of steel tubes filled with high strength concrete. Can J Civil Eng 1994; 21(2): 207-218.
[11] Silva A, Jiang Y, Castro J.M., Silvestre N, Monteiro R. Experimental assessment of the flexural behaviour of circular rubberized concrete-filled steel tubes. J Construct Steel Res 2016; 122, 557-570.
[12] Xiong MX, Xiong DX, Liew JYR. Flexural performance of concrete filled tubes with high tensile steel and ultra-high strength concrete. J Construct Steel Res 2017; 132: 191-202.
[13] Liew JR, Xiong MX. Design guide for concrete filled tubular members with high strength materials to Eurocode 4. Research Publishing, 2015.
[14] Chan TM, Huai YM, Wang W. Experimental investigation on lightweight concrete-filled cold-formed elliptical hollow section stub columns. J Construct Steel Res 2015: 115, 434-444.

[15] Liu F, Wang Y, Chan, TM. Behaviour of concrete-filled cold-formed elliptical hollow sections with varying aspect ratios. Thin-Walled Struct, 2017; 110, 47-61.
[16] Sheehan T, Dai XH, Chan TM, Lam D. Structural response of concrete-filled elliptical steel hollow sections under eccentric compression. Eng Struct 2012; 45, 314–323.
[17] Yang H, Liu F, Chan TM, Wang W. Behaviours of concrete-filled cold-formed elliptical hollow section beam-columns with varying aspect ratios. Thin-Walled Struct 2017; 120, 9-28.
[18] Slocum RM. Considerations in the design and fabrication of tubular steel transmission structures. Proceedings of the Fifteenth International Symposium on Tubular Structures - ISTS 15, 27–29 May 2015, Rio de Janeiro, Brazil.
[19] Chen JB, Chan TM, Su R KL, Castro JM. Experimental assessment on the cyclic behaviour of concrete filled steel tubular beam-columns with octagonal sections. Eng Struct 2019; 180: 544-560.
[20] Zhu JY, Chan TM. Behaviour of polygonal-shaped steel-tube columns filled with high-strength concrete. P. I. Civil Eng-Str & B 2017; 171 (SB2): 96-112.
[21] Zhu JY, Chan TM. Experimental investigation on octagonal concrete filled steel stub columns under uniaxial compression. J Construct Steel Res 2018; 147: 457-467.
[22] ANSI/AISC 341-16. Seismic provisions for structural steel buildings. Chicago: American Institute of Steel Construction (AISC); 2016.
[23] EN 1998-1:2004. Design of structures for earthquake resistance. Part 1: general rules, seismic actions and rules for buildings. CEN (European Committee for Standardization); 2004.
[24] Zhu JY, Chan TM, Young B. Cross-sectional capacity of octagonal tubular steel stub columns under uniaxial compression. Eng Struct 2019; 184: 480-494.
[25] EN ISO 6892-1:2016. Metallic materials — Tensile testing. Part 1: Method of test at room temperature. CEN (European Committee for Standardization); 2016.
[26] EN 12390-3:2009. Testing hardened concrete. Part 3: Compressive strength of test specimens. CEN (European Committee for Standardization); 2009.
[27] SAC. Protocol for Fabrication, Inspection, Testing, and Documentation of Beam-column Connection Tests and Other Experimental Specimens. Rep. No. SAC/BD-97, 1997.
[28] Liao FY, Han LH, Tao Z, Rasmussen KJ. Experimental behavior of concrete-filled stainless steel tubular columns under cyclic lateral loading. J Struct Eng 2016; 143(4), 04016219.
[29] Roeder CW, Lehman DE, Bishop E. Strength and stiffness of circular concrete-filled tubes. J Struct Eng 2010; 136(12): 1545-1553.
[30] Rahnama M, Krawinkler H. Effect of soft soils and hysteresis models on seismic design spectra. Rep. No. TB 108, The John A. Blume Earthquake Engineering Center, Stanford Univ., Stanford, CA, 1993.
[31] Ibarra LF, Medina RA, and Krawinkler H. Hysteretic models that incorporate strength and stiffness deterioration. Earthquake Eng. Struct. Dyn., 2005; 34(12), 1489–1511.
[32] Lignos DG, Krawinkler H. Deterioration Modeling of Steel Components in Support of Collapse Prediction of Steel Moment Frames under Earthquake Loading. J Struct Eng 2011; 137, 1291-1302.

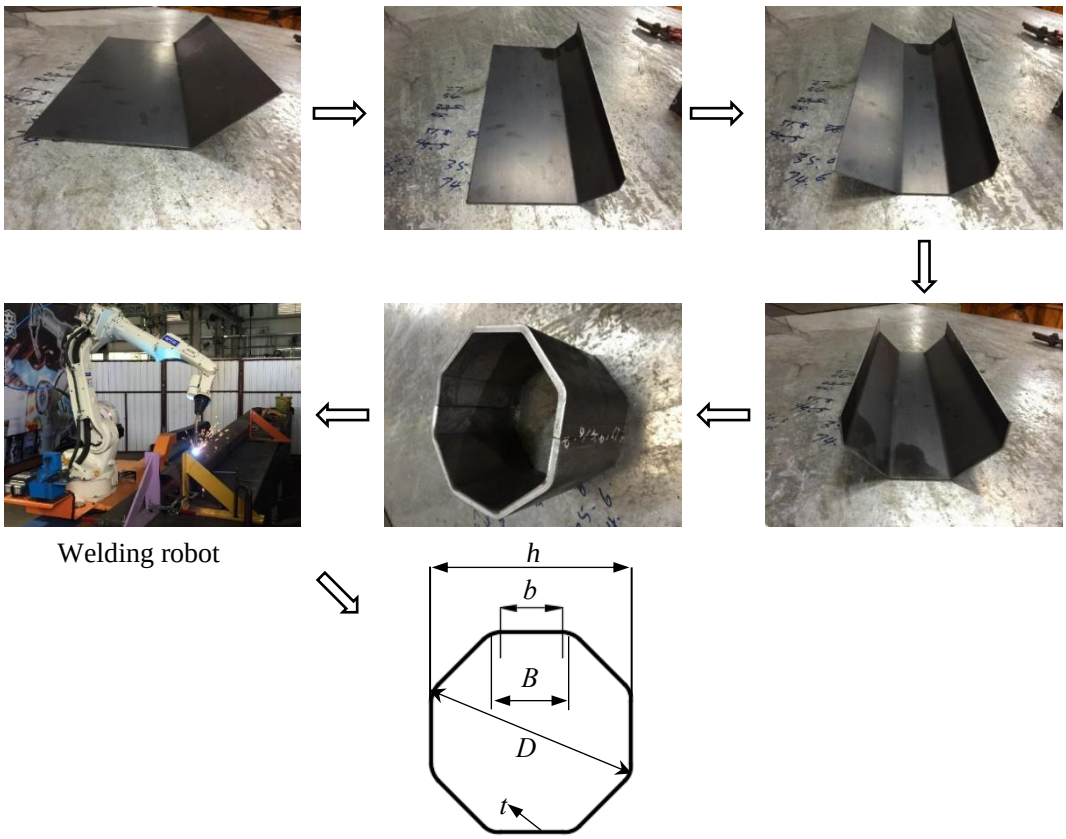

Fig. 1. Fabrication of the octagonal steel tube (adopted from Chen et al. [19]).

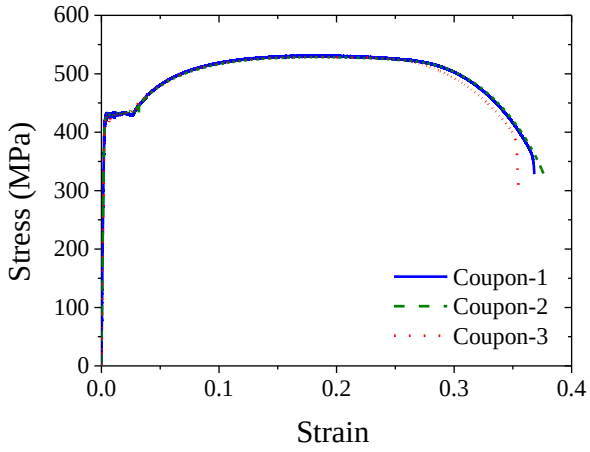

Fig. 2. Stress-strain curves of coupon tests.

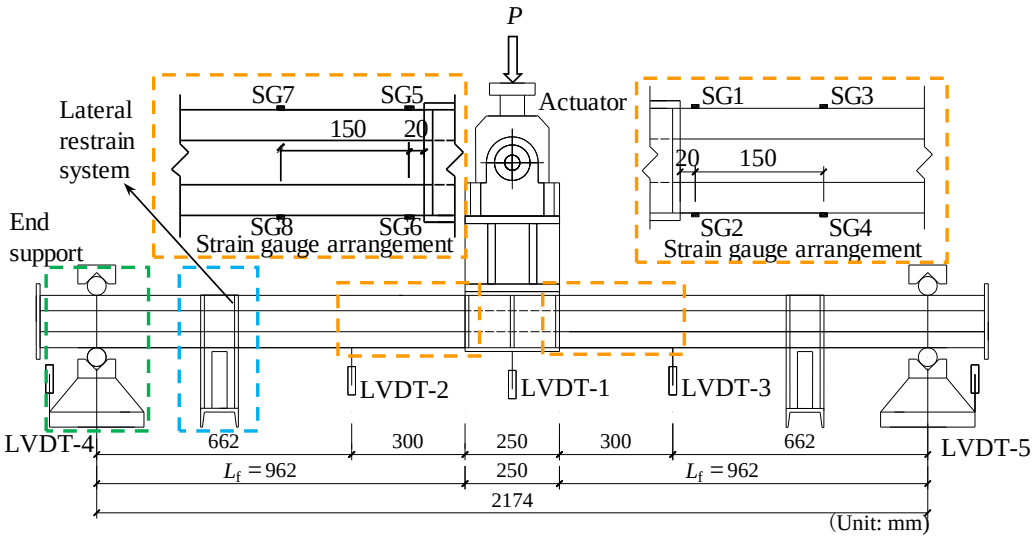

(a) Schematic view

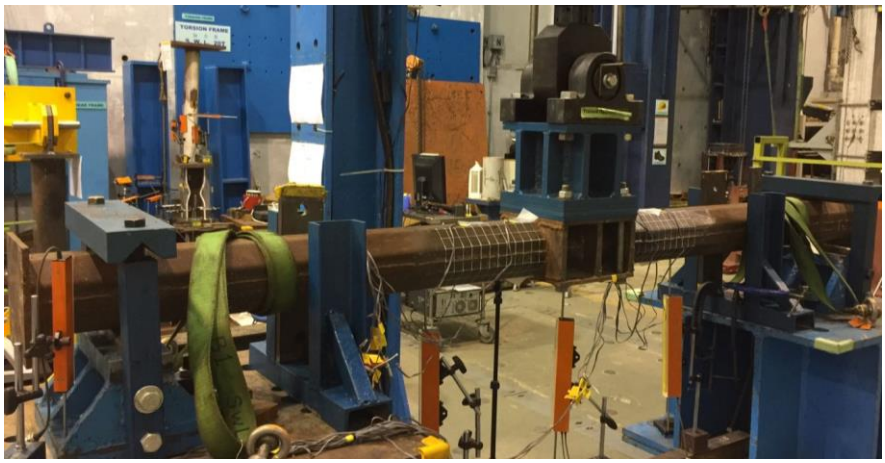

(b) Experimental view

(c) Lateral restrain system

(d) End support

Fig. 3. Schematic and experimental views of the test setup (Unit: mm).

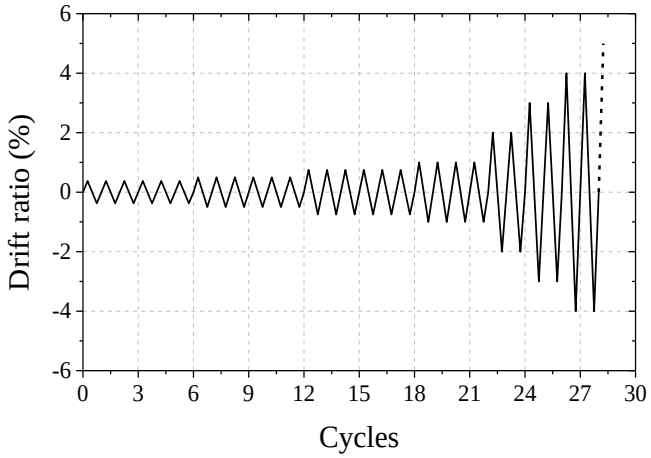

Fig. 4. Loading protocol.

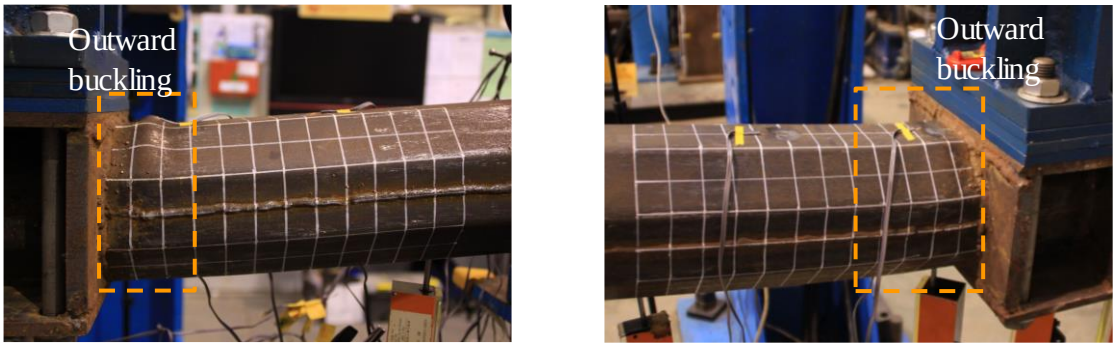

(a) Outward local buckling of hollow specimen (b) Outward local buckling of OCFST specimen

Fig. 5. Typical failure modes of specimens under monotonic loading.

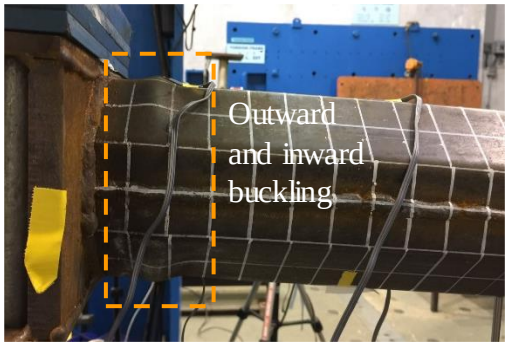

(a) Outward and inward local buckling of hollow specimen

(b) Outward local buckling and steel fracture of OCFST specimen

Fig. 6. Typical failure modes of specimens under cyclic loading.

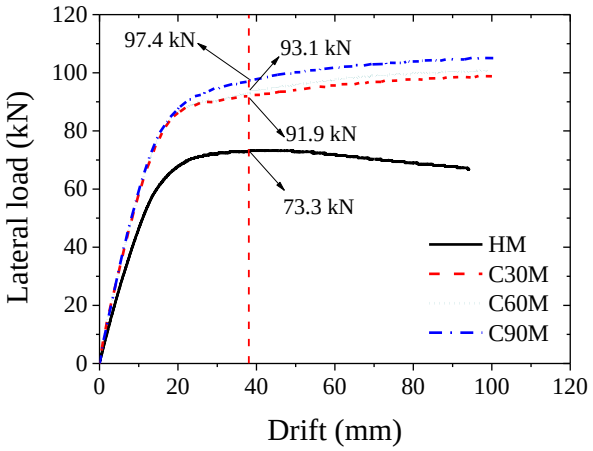

Fig. 7. Lateral load *vs* drift curves of monotonic tests.

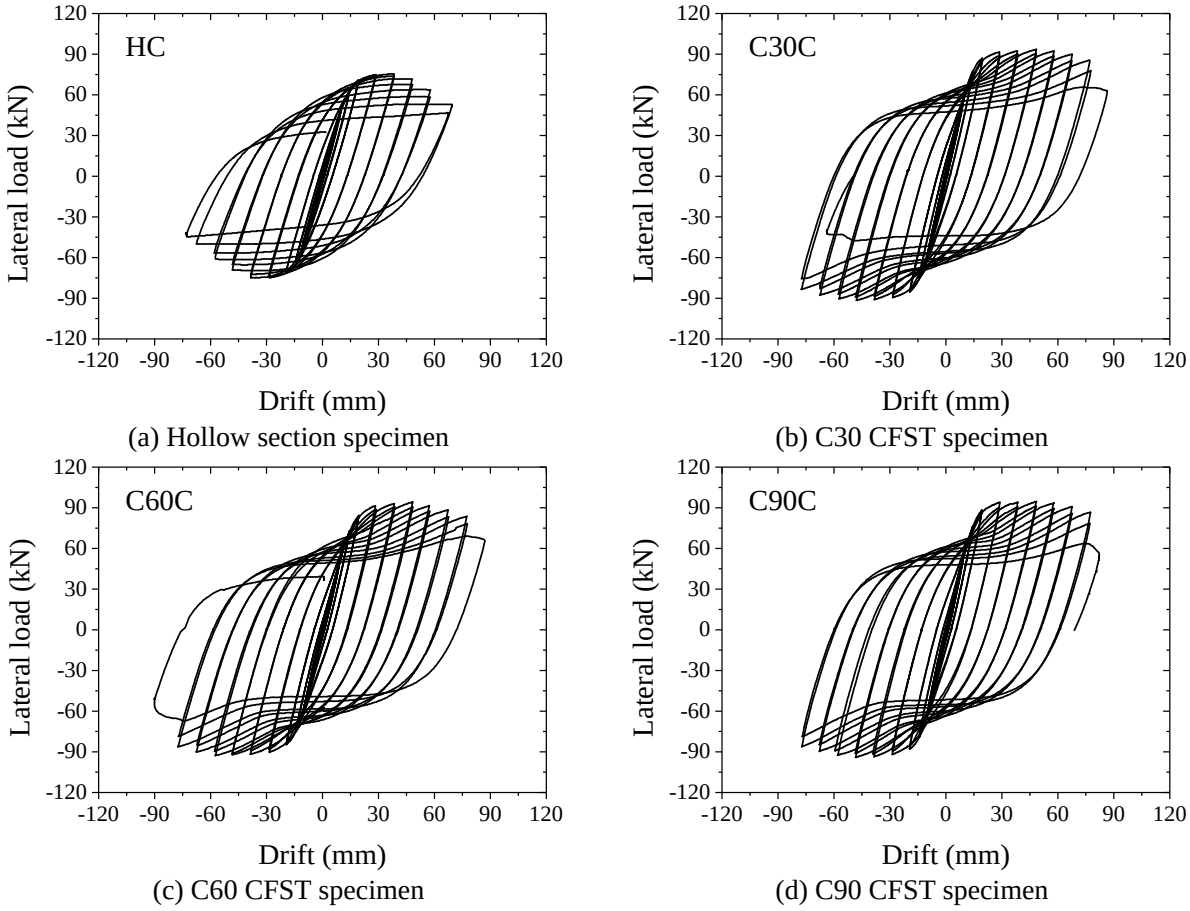

(a) Hollow section specimen (b) C30 CFST specimen

(c) C60 CFST specimen (d) C90 CFST specimen

Fig. 8. Lateral load *vs* drift curves of cyclic tests.

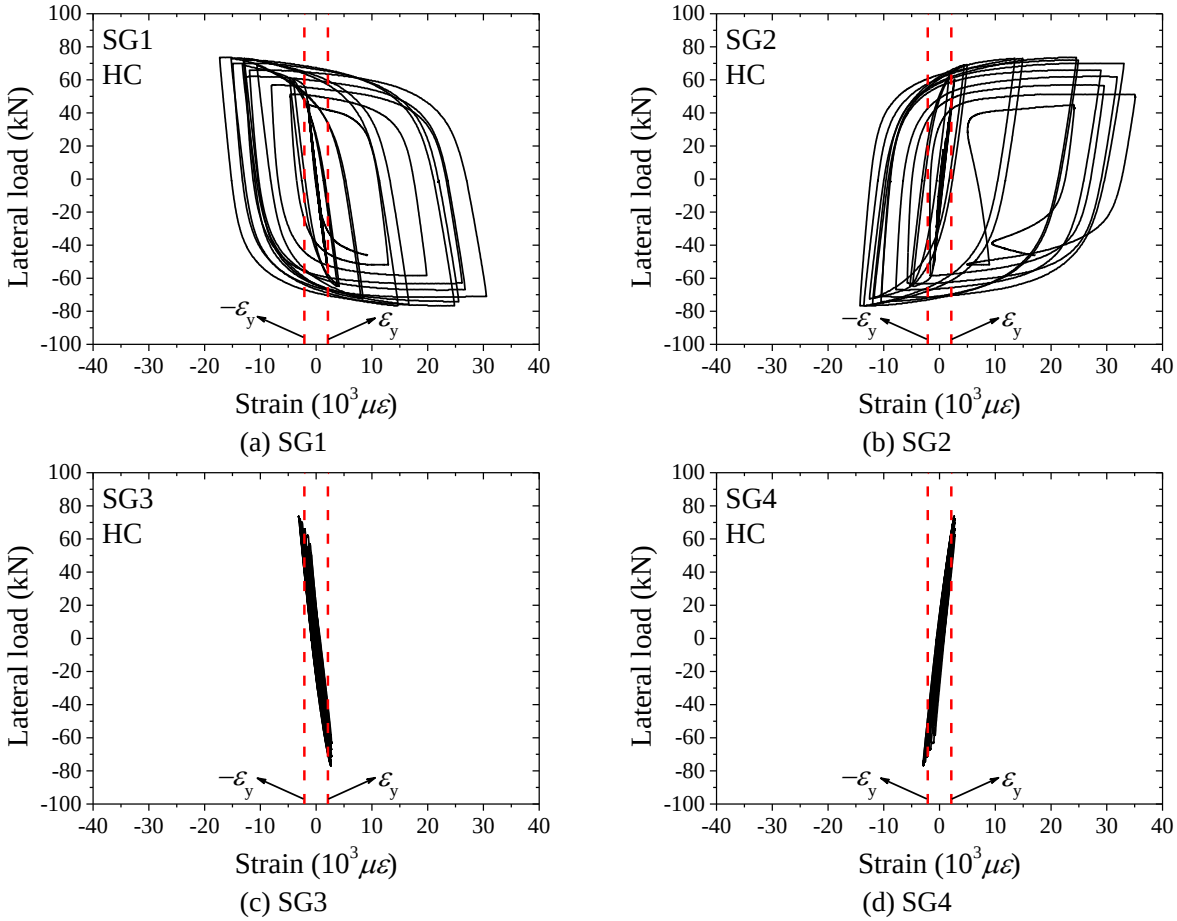

Fig. 9. Lateral load *vs* steel strains in the HC specimen.

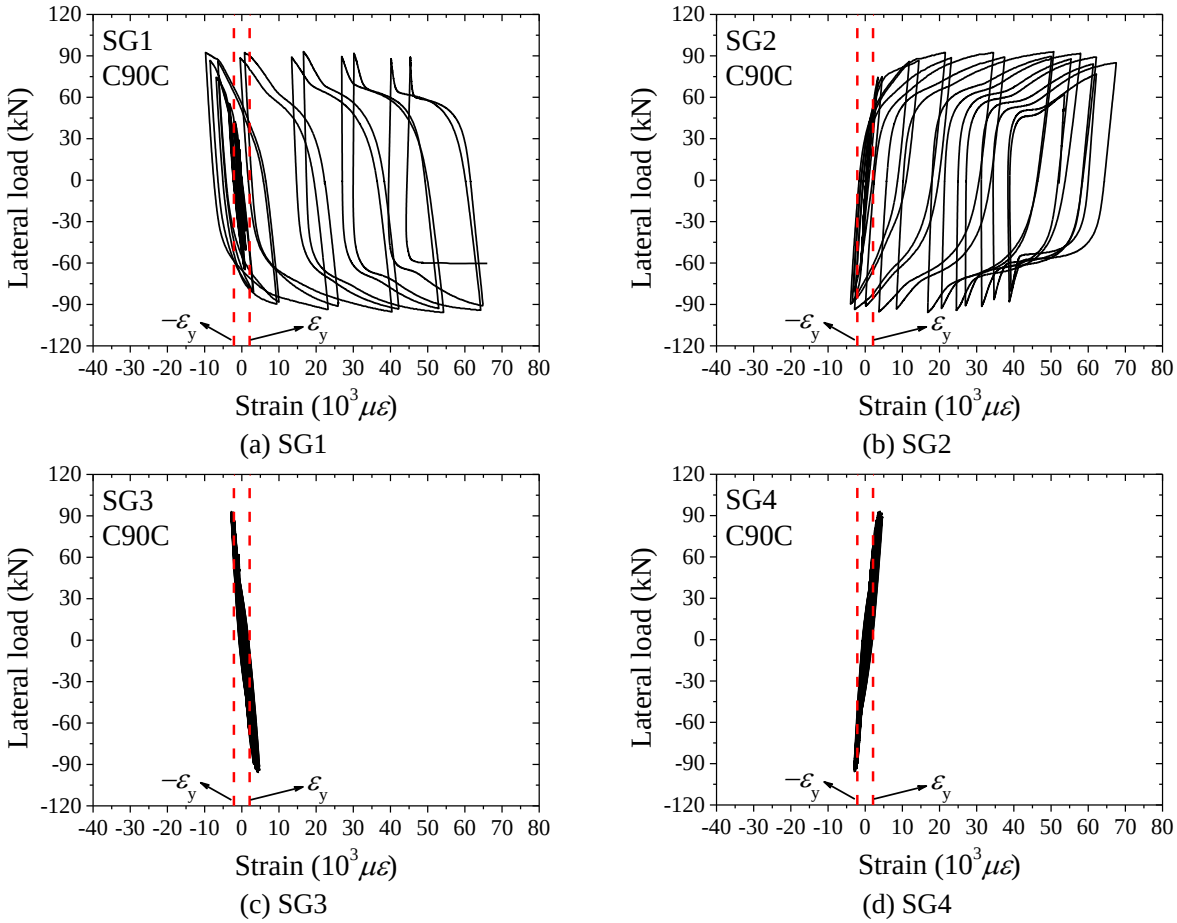

Fig. 10. Lateral load *vs* steel strains in the C90C specimen.

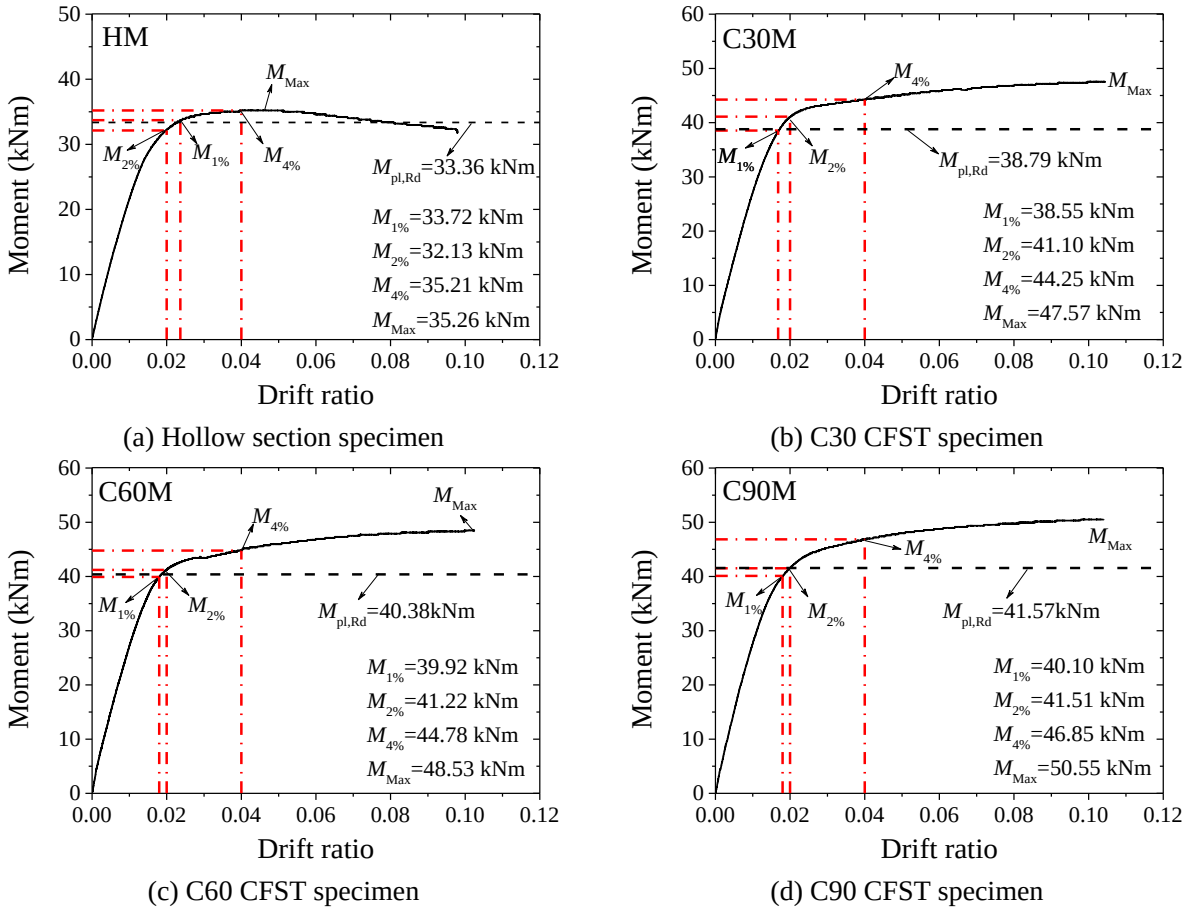

(a) Hollow section specimen

(b) C30 CFST specimen

(c) C60 CFST specimen

(d) C90 CFST specimen

Fig. 11. Monotonic moment *vs* drift ratio curves.

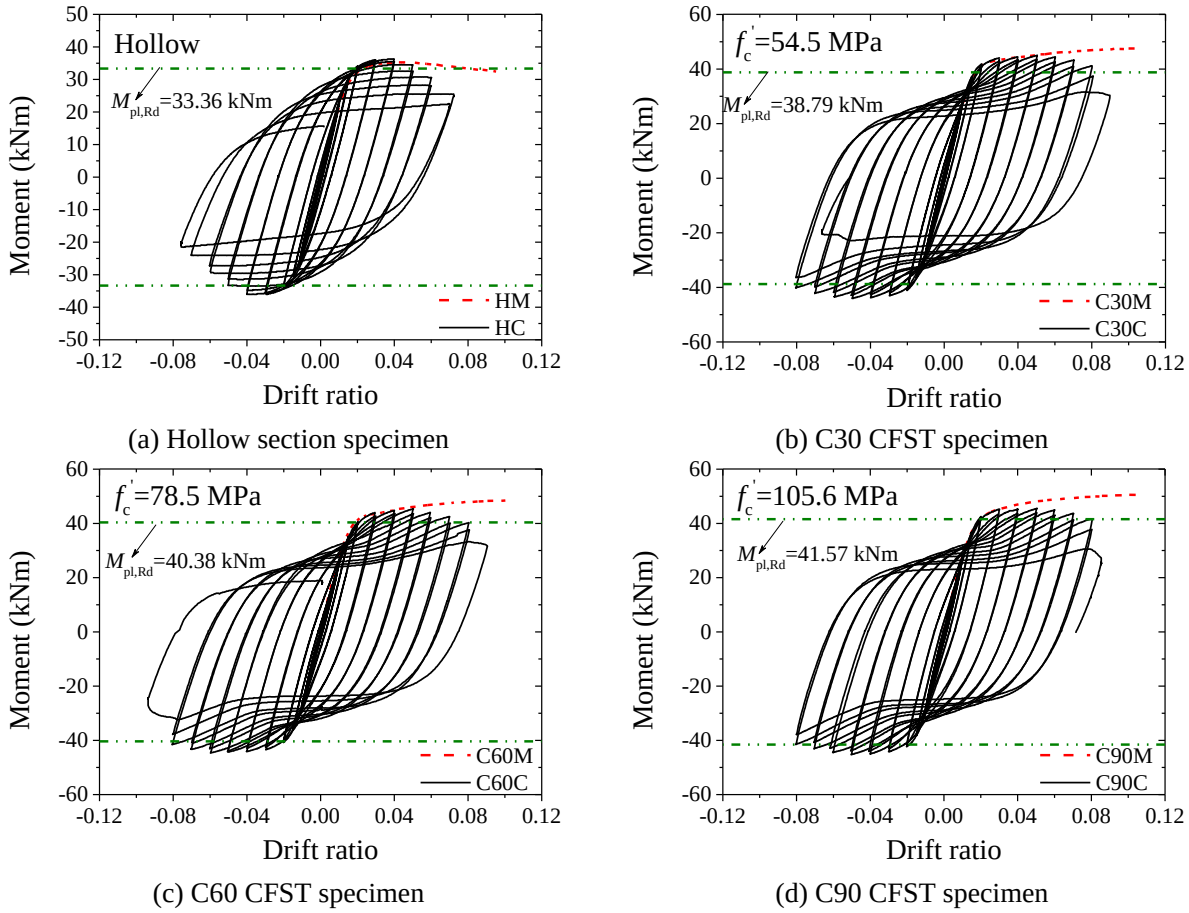

Fig. 12. Moment *vs* drift ratio hysteretic curves.

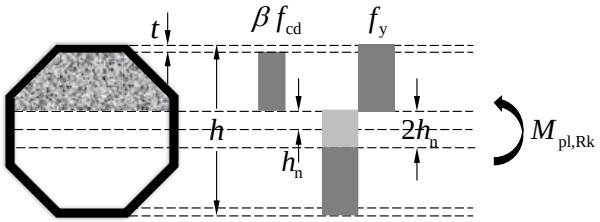

Fig. 13. Plastic stress distributions under pure bending according to EN 1994-1-1 [6].

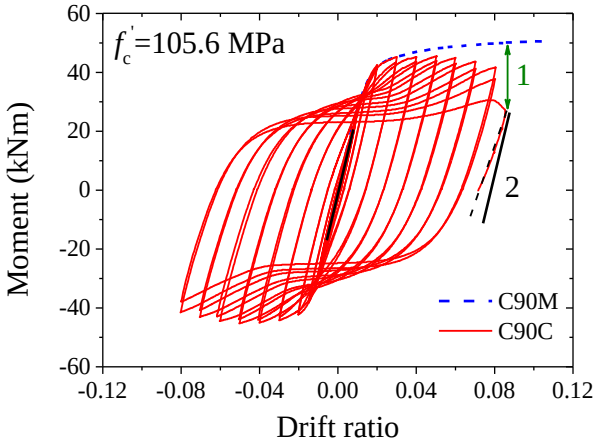

Fig 14. Monotonic and cyclic experimental results of OCFST beams.

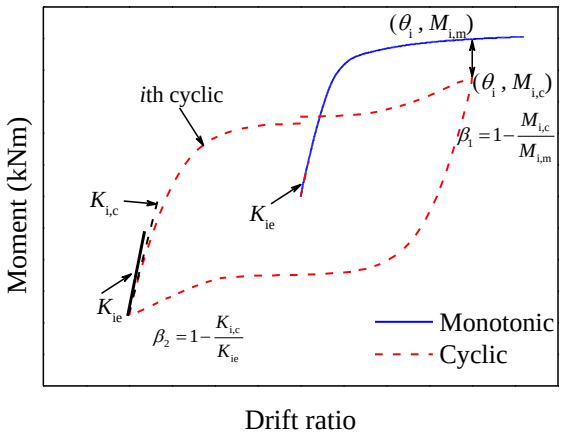

Fig 15. Determination of the deteriorations of strength and stiffness.

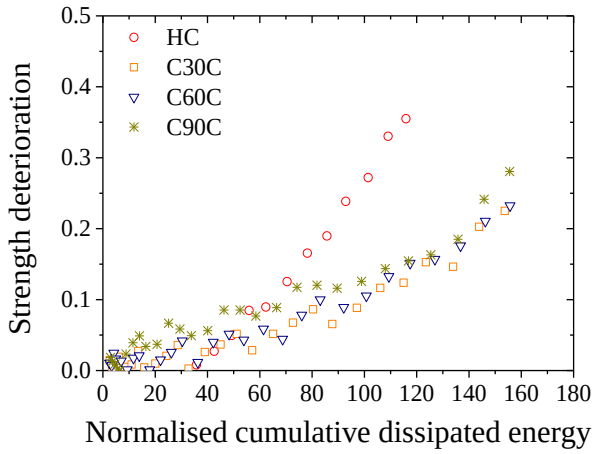

(a) Strength deterioration

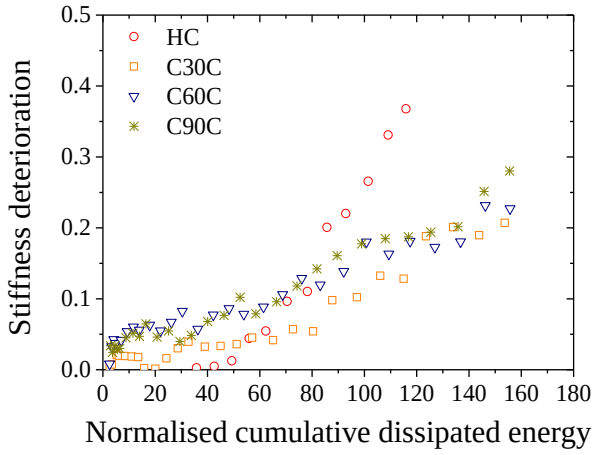

(b) Stiffness deterioration

Fig 16. Deteriorations observed from the OCFST beam cyclic tests.

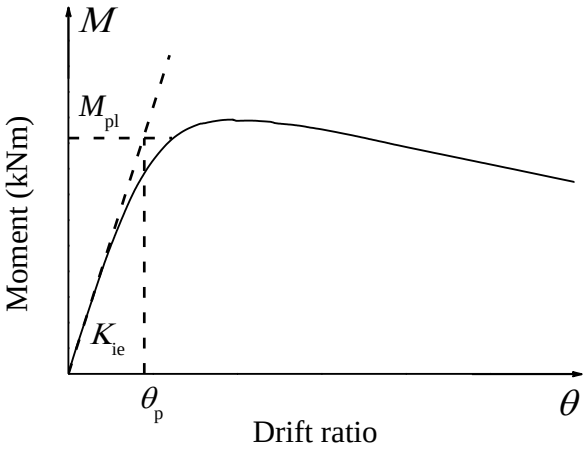

Fig. 17. Typical moment *vs* drift ratio curve.

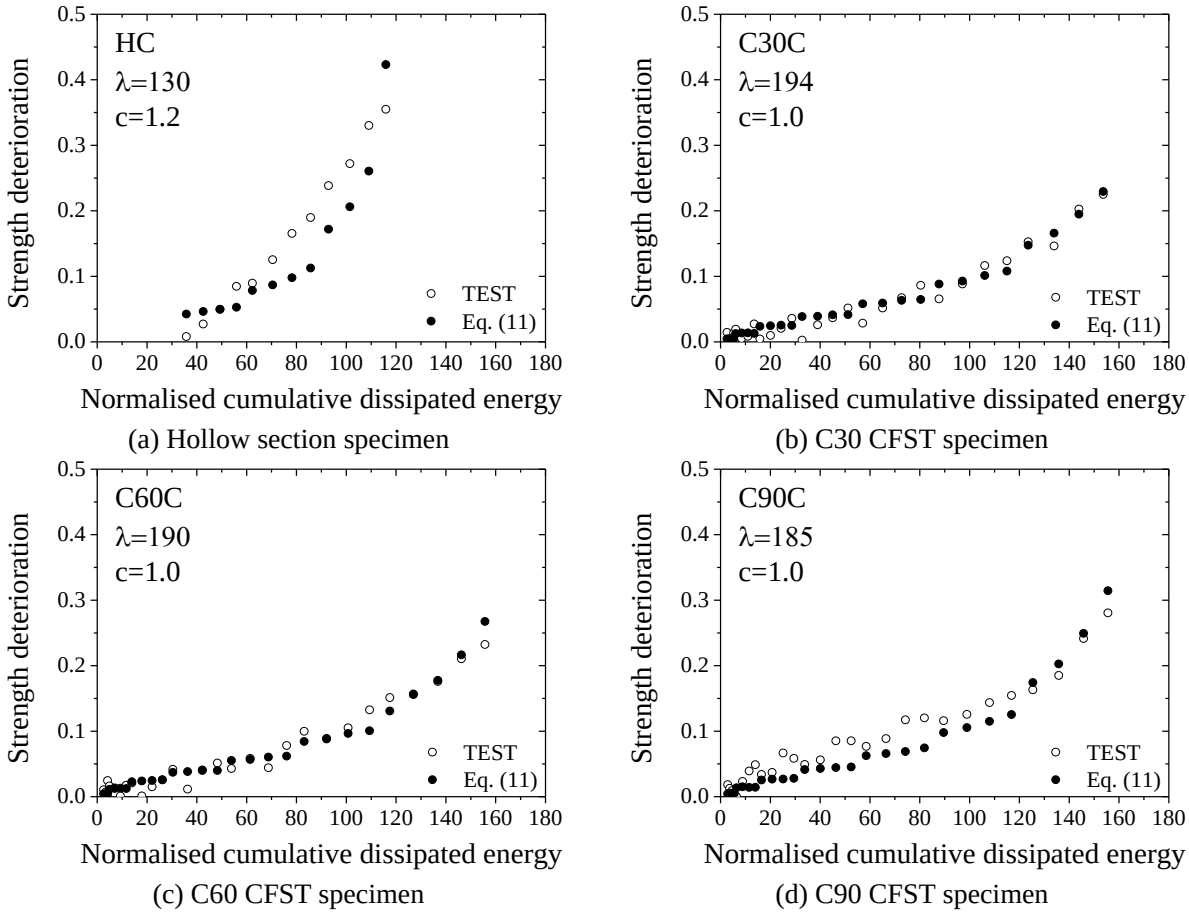

Fig 18. Comparisons of the strength deteriorations.

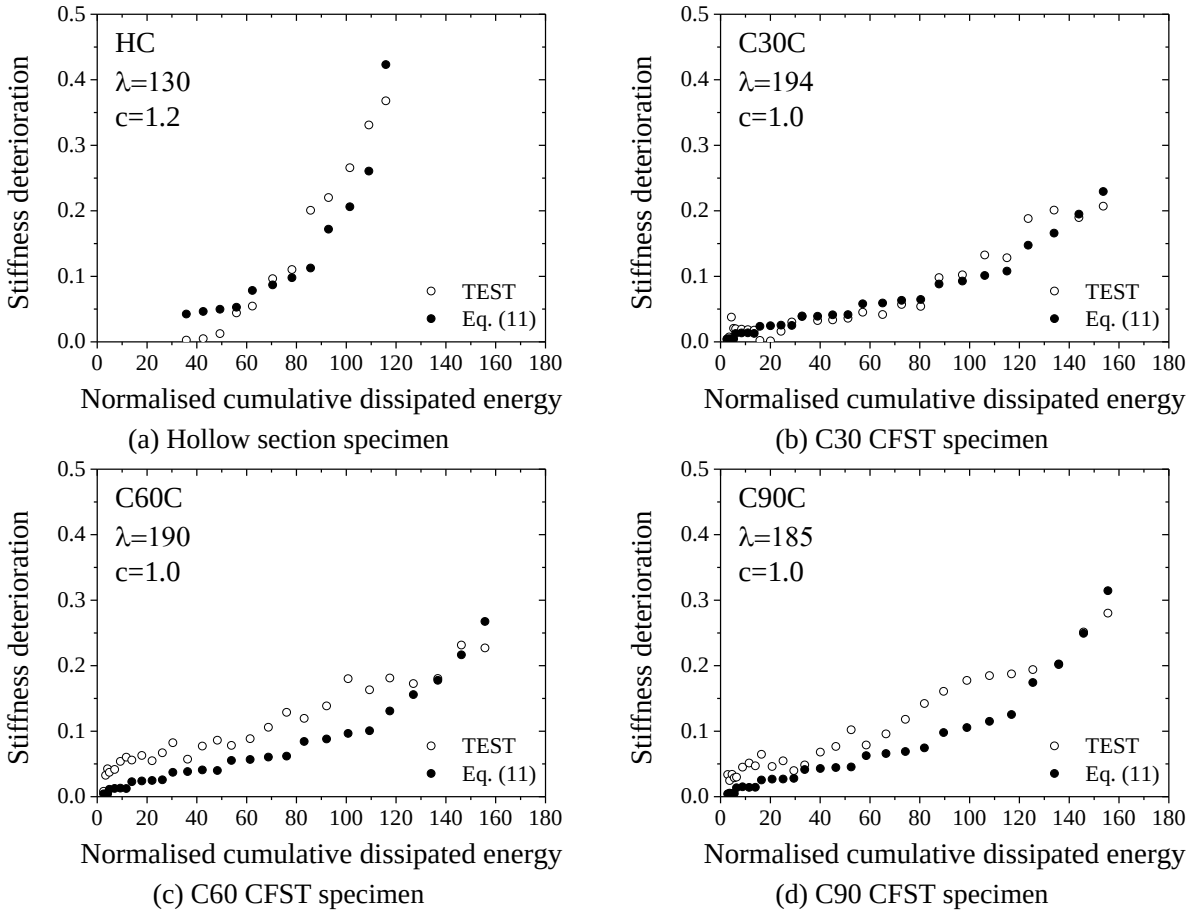

Fig 19. Comparisons of the stiffness deteriorations.

Table 1. Detailed information of test specimens.

Specimen	D mm	H mm	B mm	b mm	t mm	E_c GPa	f_c' MPa	E_s GPa	f_y MPa	b/t -	δ
HM	148.66	139.70	57.87	49.58	3.95	-	-	200.1	423.2	12.6	-
HC	149.08	140.10	58.03	49.75	3.94	-	-	200.1	423.2	12.6	-
C30M	148.59	139.63	57.84	49.55	3.94	27.1	54.5	200.1	423.2	12.6	0.47
C30C	148.99	139.01	57.58	49.30	3.95	27.1	54.5	200.1	423.2	12.5	0.47
C60M	148.82	139.85	57.93	49.64	3.94	33.0	78.5	200.1	423.2	12.6	0.38
C60C	148.98	140.00	57.99	49.71	3.94	33.0	78.5	200.1	423.2	12.6	0.38
C90M	149.12	140.13	58.04	49.76	3.94	36.5	105.6	200.1	423.2	12.6	0.32
C90C	148.17	139.24	57.68	49.39	3.95	36.5	105.6	200.1	423.2	12.5	0.32

Table 2. Results of tensile coupon tests.

Coupon	E_s GPa	f_y MPa	f_u MPa	ε_y $\mu\varepsilon$	ε_{st} %	ε_u %	ε_f %
1	195.9	424.8	531.4	2168	2.71	18.34	36.83
2	201.5	427.7	528.9	2123	2.94	18.18	37.88
3	202.8	417.1	529.5	2057	2.89	17.69	35.23
Average	***200.1***	***423.2***	***529.9***	***2116***	***2.85***	***18.07***	***36.65***

Table 3. Concrete mix proportions.

Grades	Water/ cement	Water	Cement	Fly ash	Silica Fume	Sand	Aggregate (mm)		S.P.*
							5-10	10-20	
	-	kg/m^3	kg/m^3	kg/m^3	kg/m^3	kg/m^3	kg/m^3	kg/m^3	kg/m^3
C30	0.55	220	400	0	0	810	840	0	3.78
C60	0.33	180	412	138	0	800	235	570	7.58
C90	0.27	156	360	190	33	765	795	0	13.4

Note: *. S.P. is superplasticizer.

Table 4. Comparison of the bending moments of monotonic specimens.

Speci-mens	Experimental results				EN 1994-1-1				AISC 360-16			
	$M_{1\%}$	$M_{2\%}$	$M_{4\%}$	M_{Max}	$M_{pl,Rd}$	$M_{1\%}$ / $M_{pl,Rd}$	$M_{2\%}$ / $M_{pl,Rd}$	M_{max} / $M_{pl,Rd}$	M_{AISC}	$M_{1\%}$ / M_{AISC}	$M_{2\%}$ / M_{AISC}	M_{max} / M_{AISC}
	kNm	kNm	kNm	kNm	kNm	-	-	-	kNm	-		-
HM	33.72	32.13	35.21	35.26	33.36	1.011	0.963	1.057	33.36	1.011	0.963	1.057
C30M	38.55	41.10	44.25	47.57	38.79	0.994	1.060	1.226	38.66	0.997	1.063	1.230
C60M	39.92	41.22	44.78	48.53	40.38	0.989	1.021	1.202	39.84	1.002	1.035	1.218
C90M	40.10	41.51	46.85	50.55	41.57	0.965	0.999	1.216	40.92	0.980	1.014	1.235
Mean						**0.989**	**1.011**	**1.175**		**0.997**	**1.019**	**1.185**
COV						**0.019**	**0.040**	**0.068**		**0.013**	**0.041**	**0.072**

Table 5. Comparison of the bending moments of cyclic specimens.

Specimens	Experimental results		EN 1994-1-1			AISC 360-16		
	$M_{1\%}$	M_{ue}	$M_{pl,Rd}$	$M_{1\%} / M_{pl,Rd}$	$M_{ue} / M_{pl,Rd}$	M_{AISC}	$M_{1\%} / M_{AISC}$	M_{ue} / M_{AISC}
	kNm	kNm	kNm	-	-	kNm	-	-
HC	33.26	37.50	33.38	0.996	1.123	33.38	0.996	1.113
C30C	39.74	44.54	38.75	1.026	1.149	38.37	1.036	1.161
C60C	40.23	45.05	40.47	0.994	1.113	39.93	1.008	1.128
C90C	41.01	45.43	41.09	0.998	1.106	40.45	1.014	1.123
Mean				**1.004**	**1.123**		**1.014**	**1.131**
COV				**0.015**	**0.017**		**0.017**	**0.018**

Table 6. Comparison of the flexural stiffness.

Specimens	Experimental results		EN 1994-1-1		AISC 360-16	
	K_{ie} kNm·m	E_h kNm	K_{icEC} (kNm·m)	K_{ie}/K_{icEC} -	K_{icAISC} (kNm·m)	K_{ie}/K_{icAISC} -
HM	1867	-	1732	1.078	1732	1.078
HC	1927	36.67	1732	1.113	1732	1.113
C30M	2237	-	2170	1.031	2279	0.982
C30C	2270	54.40	2170	1.046	2279	0.996
C60M	2324	-	2281	1.019	2428	0.957
C60C	2367	54.84	2281	1.038	2428	0.975
C90M	2570	-	2349	1.094	2523	1.019
C90C	2571	55.41	2349	1.095	2523	1.019
Mean				**1.064**		**1.017**
COV				**0.033**		**0.052**